Inorganic Chemistry

Article

pubs.acs.org/IC

Microwave-Solvothermal Synthesis of Various Polymorphs of Nanostructured TiO_2 in Different Alcohol Media and Their Lithium Ion Storage Properties

Sukeun Yoon, Eun-Sung Lee, and Arumugam Manthiram*

Electrochemical Energy Laboratory Materials Science and Engineering Program, University of Texas at Austin, Austin, Texas 78712, United States

ABSTRACT: The various polymorphs (anatase, rutile, and brookite) of TiO_2 with different nanomorphologies have been synthesized by a facile microwave-assisted solvothermal process without surfactants, employing $TiCl_4$ or $TiCl_3$ as precursors in various alcohol (ethanol, propanol, butanol, and octanol) media. The samples have been characterized by X-ray diffraction (XRD), electron microscopy, and Brunauer–Emmett–Teller (BET) surface area analysis. The Ti/Cl ion concentration, reaction pH, and size of the alcohol molecule are found to control the morphology, crystal structure, and crystallite size of the TiO_2 particles. Among the various TiO_2 polymorphs synthesized, the rutile TiO_2 spheres built up of nanorods that were synthesized with $TiCl_4$ in octanol have an average pore size and surface area of, respectively, 5 nm and 404 m^2/g and exhibit the best electrochemical performance with a capacity of >200 mAh/g after 100 cycles and high rate capability. The excellent electrochemical properties originate from the nanorod-building morphology and mesoporosity of TiO_2 spheres that provide good electrical contact, accommodates the strain smoothly, and facilitates facile lithium-ion diffusion.

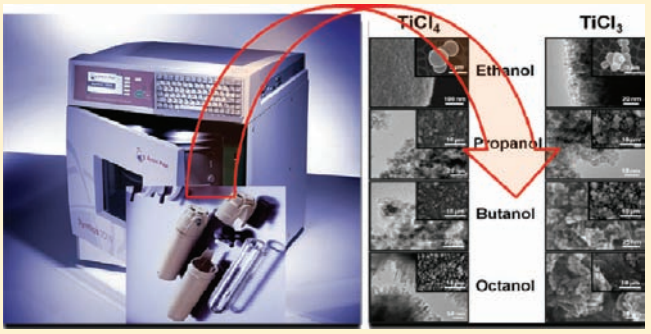

1. INTRODUCTION

As an electrochemical energy storage device, lithium-ion batteries have become the dominant power source for portable electronic devices due to their high energy density. They are now being pursued intensively for automotive and stationary storage applications. However, the currently used lithium-ion batteries cannot quite meet the requirements of the automotive and stationary storage sectors, in terms of power density, cycle life, and safety. Particularly, the currently used graphite anode with a capacity of 372 mAh/g suffers from safety concerns arising from formation of a solid–electrolyte interfacial (SEI) layer by reaction of the graphite surface with the electrolyte and consequent plating of lithium on the SEI layer under high rates of charge–discharge as its charge–discharge potential is close to that of Li/Li^+.[1,2] This difficulty has generated interest in anode materials with operating voltages well above that of Li/Li^+. In this regard, crystalline TiO_2 with a theoretical capacity of 335 mAh/g has become appealing due to the higher operating voltage (~1.5 V vs Li/Li^+), absence of SEI layer formation, excellent safety characteristics, abundance, and low toxicity of Ti.[3−5]

TiO_2 is known to crystallize in various polymorphic modifications: rutile, brookite, TiO_2(B), and anatase.[6−18] The rutile form is the thermodynamically more stable phase under standard conditions. Unfortunately, only a small amount of lithium (0.1–0.25 per formula) could be reversibly inserted into micrometer-size particles of rutile. The brookite phase is the least stable and difficult to prepare, so only a few studies are available on its use as an anode in lithium-ion batteries. On the other hand, the kinetics of reaction of microfibrous TiO_2(B) with lithium ions has recently been reported to be controlled by a pseudocapacitive faradaic process. Anatase phase is metastable, but it is the most extensively studied form as an anode for lithium-ion batteries.

Interestingly, the lithium insertion/extraction kinetics could be enhanced significantly by adopting nanostructured TiO_2. Nanostructured TiO_2 with a large surface area can accommodate smoothly the strain occurring during cycling, and easy access to electrolyte can lead to a reduced diffusion pathway for electronic/ionic transport, resulting in excellent power density. However, the nanostructure could lead to a decrease in volumetric energy density and an increase in side reactions due to the high electrolyte/electrode surface area.[19−21] Accordingly, a variety of approaches have been pursued to obtain TiO_2 as nanorods, nanowires, nanotubes, and nanoflowers by employing precipitation, hydrothermal, sol–gel, and templating methods.[5,7−18,22]

We present here a facile microwave-assisted solvothermal process to obtain the various polymorphs of TiO_2 that exhibit good cycling performance and high rate capability. The microwave-assisted hydrothermal (MW-HT) and solvothermal (MW-ST) methods offer a clean, low-cost approach to obtain nanocrystals within a very short reaction time (in minutes) with

Received: October 15, 2011
Published: March 1, 2012

 © 2012 American Chemical Society dx.doi.org/10.1021/ic202239n | *Inorg. Chem.* 2012, 51, 3505–3512

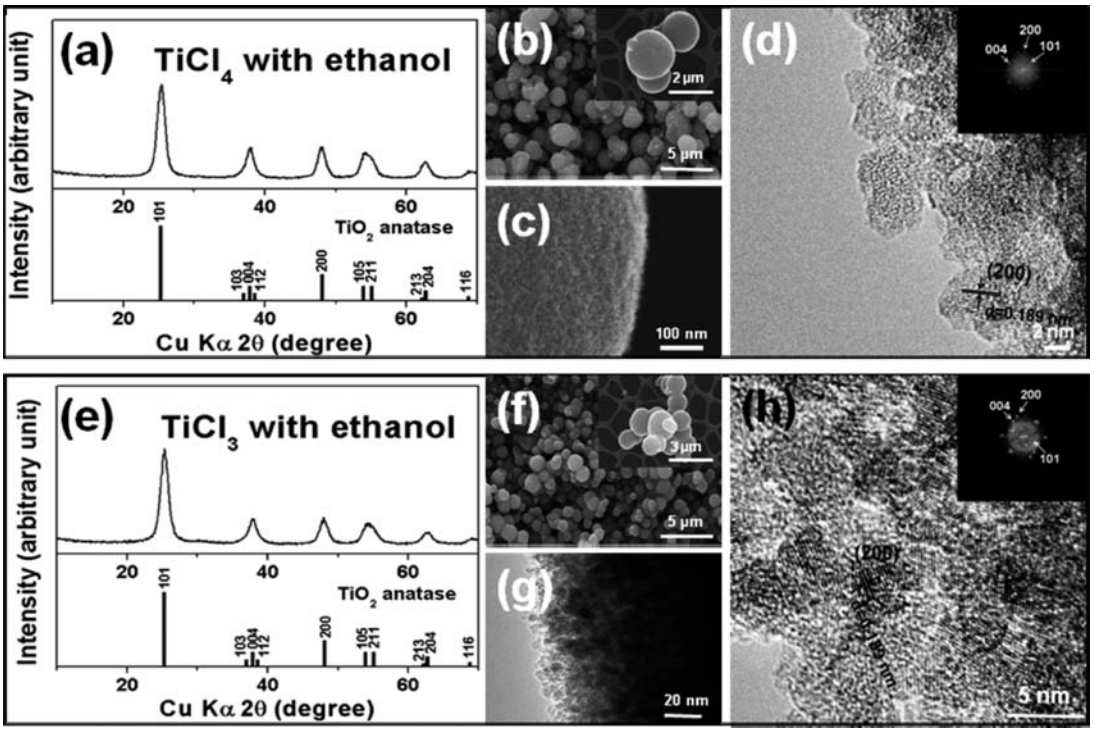

Figure 1. (a) XRD pattern, (b and c) SEM images, and (d) TEM and FFT (inset) images of the TiO_2 spheres synthesized with $TiCl_4$ and ethanol, and (e) XRD pattern, (f) SEM image, and (g and h) TEM and FFT (inset) images of the TiO_2 spheres synthesized with $TiCl_3$ and ethanol.

high yields.[23] The synthesized nanostructured TiO_2 samples are characterized by X-ray diffraction (XRD), Brunauer–Emmett–Teller (BET) surface area measurement, electron microscopy, and electrochemical charge–discharge measurements.

2. EXPERIMENTAL SECTION

The nanostructured TiO_2 samples were obtained by a microwave-assisted solvothermal reaction without any surfactants. In a typical experiment, 1 mmol of the titanium precursor (titanium trichloride ($TiCl_3$ in 20% HCl) or titanium tetrachloride ($TiCl_4$ in 20% HCl)) was added to 25 mL of one of the alcohols (ethanol, propanol, butanol, or octanol) under mild stirring for 6 h. The transparent solution thus formed was transferred into quartz vessels and loaded into an Anton Paar microwave synthesis system (Synthos-3000). The microwave system was operated at a frequency of 2.45 GHz and power of 600 W, the sample temperature was ramped to 190 °C and kept at 190 °C for 30 min. After the MW-HT process, the resultant slurry was filtered, washed with deionized water and acetone, and dried in a vacuum oven at 80 °C.

Phase analysis of the synthesized samples was performed with a Phillips X-ray diffractometer and Cu Kα radiation. The specific surface areas were evaluated with a Quantachrome surface analyzer based on the Brunauer–Emmett–Teller (BET) multipoint method and N_2 physisorption at 77 K. Adsorption–desorption isotherm measurements were used to determine the porosity and pore size distribution using the Barrett–Joyner–Halenda (BJH) method. The morphology, microstructure, and composition of the synthesized powders were examined with a Hitachi S-5500 scanning transmission electron microscope (STEM) and JEOL 2010F transmission electron microscope (TEM).

Electrodes for electrochemical evaluation were prepared by mixing 70 wt % active material (TiO_2) powder, 15 wt % carbon black (Super P) as a conducting agent, and 15 wt % polyvinylidenefluoride (PVDF) dissolved in *N*-methylpyrrolidone (NMP) as a binder to form a slurry, followed by coating on a copper foil, pressing, and drying at 120 °C for 3 h under vacuum. The CR2032 coin cells were assembled in an Ar-filled glovebox using Celgard polypropylene as a separator, lithium foil as the counter electrode, and 1 M $LiPF_6$ in ethylenecarbonate (EC)/diethylcarbonate (DEC) (1:1 v/v) as the electrolyte. The charge–discharge experiments were performed galvanostatically at a constant current density of 30 mA/g of active material within the voltage range of 1–3 V vs Li/Li^+.

3. RESULTS AND DISCUSSION

3.1. Synthesis and Characterization. Our first set of experiments was carried out with ethanol. Ethanol mixes homogeneously with $TiCl_4$ or $TiCl_3$ under mild stirring due to its polarity and smaller size. Figure 1a shows the XRD pattern of the as-synthesized samples prepared with $TiCl_4$. It could be indexed on the basis of tetragonal anatase TiO_2 ($I4_1/amd$, JCPD 21-1272) without any reflections corresponding to impurity phases. The mean crystallite size D_{101} calculated based on the (101) reflection using Scherer's equation is ~7.5 nm. The SEM images shown in Figure 1b and 1c reveal spherical morphology with an average particle size of ~1 μm. The selected individual single particle in Figure 1c clearly reveals a rough surface, possibly with the existence of a large number of mesopores on the sphere surface. The mesopores may have a 3-dimensionally interconnected framework that is built by the nanosize TiO_2 building-block particles. The nanosize building-block morphology as shown by the SEM images could be beneficial to reduce the diffusion pathways for ionic and electronic transport and increase the power density. Figure 1d shows the high-resolution TEM (HRTEM) image of the anatase TiO_2 spheres, and each crystallite has an average size of ~8 nm. It also exhibits the lattice fringe with a *d*-spacing value of 0.189 nm, corresponding to the (200) plane of anatase TiO_2. The fast Fourier transform (FFT) in Figure 1d gives a set of sharp spots corresponding to the (101), (004), and (200) planes of the anatase phase, which is consistent with the XRD data.

Figure 1e shows the XRD patterns of the as-synthesized sample prepared with $TiCl_3$. It could also be indexed based on

dx.doi.org/10.1021/ic202239n | *Inorg. Chem.* 2012, 51, 3505–3512

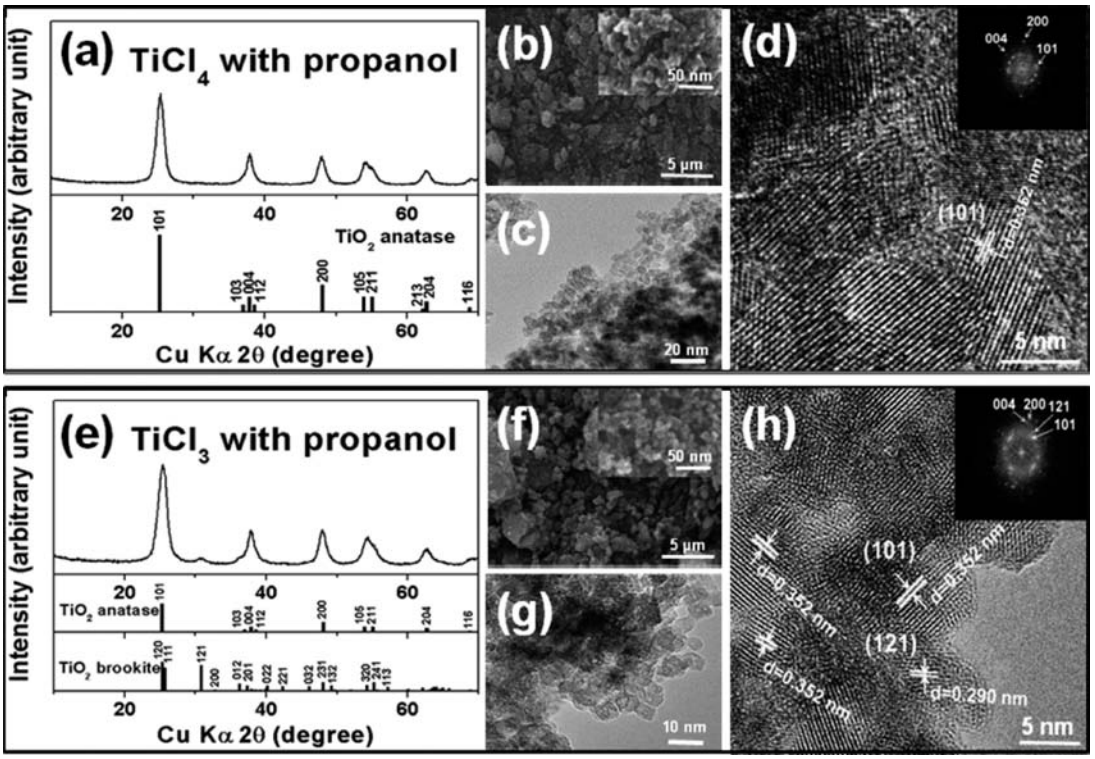

Figure 2. (a) XRD pattern, (b) SEM image, and (c and d) TEM and FFT (inset) images of the TiO_2 nanoparticles synthesized with $TiCl_4$ and propanol, and (e) XRD pattern, (f) SEM image, and (g and h) TEM and FFT (inset) images of the TiO_2 nanoparticles synthesized with $TiCl_3$ and propanol.

the tetragonal anatase TiO_2 ($I4_1/amd$, JCPD 21-1272) without any impurity phases. Unlike reaction with $TiCl_4$, reaction with $TiCl_3$ may involve oxidation and hydrolysis to form TiO_2 as the lower valent Ti^{3+} oxides will readily be oxidized to Ti^{4+} oxides. The mean crystallite size D_{101} is ~7.5 nm. The SEM image shown in Figure 1f reveals an average particle size of ~1 μm. The HRTEM image in Figure 1g indicates that each nanoparticle has an average domain size of ~10 nm, and Figure 1h shows the lattice fringe with a *d*-spacing value of 0.189 nm, corresponding to the (200) plane of anatase TiO_2. The FFT image in Figure 1h gives a set of sharp spots corresponding to the (101), (004), and (200) planes of the anatase phase.

In general, titanium cations are solvated in aqueous solution and form 6-fold-coordinated, charged complexes $[TiX_6]^{z+}$ that are influenced by the nature of the ligand X, pH of the solution, and presence of complexing agents.[13,24−26] In the MW-ST process of our study, the Ti/Cl ion concentration (chloride is strong complexing agent), pH of the solution, and effect of the alcoholic medium are considered to influence synthesis of the TiO_2 nanocrystals. During the MW-ST process, hydrolysis and ethanolysis of $TiCl_4$ or $TiCl_3$ occur simultaneously. First, $TiCl_4$ forms a complex $[Ti(OH)_nCl_m]^{2-}$ ($n + m = 6$),[19,20] which on hydrolysis produces TiO_2 embryos that act as seed for growth of TiO_2. The linkage between the $[Ti(OH)_4Cl_2]^{2-}$ complex and TiO_2 embryos takes place by a dehydration reaction.[26] Consequently, the connection of TiO_2 nanoparticles and/or formation of mesopores occurs in the TiO_2 nanoparticles. Also, ethanolysis of $TiCl_4$ or $TiCl_3$ occurs within the surrounding of TiO_2 embryos or nanoparticles, so the TiO_2 particles formed thereupon serve as the nucleation for particle aggregation.

Our second set of experiments was carried out with propanol. Propanol also mixes uniformly with $TiCl_4$ or $TiCl_3$ under mild stirring. Figure 2a shows the XRD pattern of the as-synthesized sample prepared with $TiCl_4$, and all reflections could be indexed based on the tetragonal anatase TiO_2 ($I4_1/amd$, JCPD 21-1272) without any impurity phases. The mean crystallite size D_{101} is ~7.5 nm. The SEM and TEM images shown in Figure 2b and 2c reveal an average particle size of ~15 nm. The lattice spacing (Figure 2d) of 0.352 nm matches with that for the (101) plane of anatase TiO_2. The inset in Figure 2d presents the FFT image, which gives a set of sharp spots corresponding to the (101), (004), and (200) planes of the anatase phase.

On the other hand, the XRD pattern of the as-synthesized sample prepared with $TiCl_3$ in Figure 2e indicates the presence of tetragonal anatase TiO_2 ($I4_1/amd$, JCPD 21-1272) and a small amount of orthorhombic brookite TiO_2 ($Pcab$, JCPD 29-1360). The mean crystallite size D_{101} of the anatase phase is ~6.8 nm. The SEM and TEM images shown in Figure 2f and 2g reveal an average particle size of ~10 nm. The HRTEM image in Figure 2h shows the lattice fringe is related to the (101) plane of anatase TiO_2. The inset in Figure 2h presents the FFT image, showing a set of sharp spots corresponding to the (101), (004), and (200) planes of anatase and the (121) plane of brookite phases. Although the hydrolysis reaction of $TiCl_4$ or $TiCl_3$ could occur during the MW-ST process to form the nanoparticles, the other reactions to build any specific morphology by directional growth or nanoparticle aggregation do not seem to occur. The OH^- ions were not selectively adsorbed on the hydrophilic surfaces of the particles after nucleation of amorphous nanoparticles, which leads to formation of nanoparticles.[27,28]

Our third set of experiments was carried out with butanol. Unlike ethanol and propanol, butanol does not mix homogeneously with $TiCl_4$ or $TiCl_3$ under mild stirring due

dx.doi.org/10.1021/ic202239n | *Inorg. Chem.* 2012, 51, 3505−3512

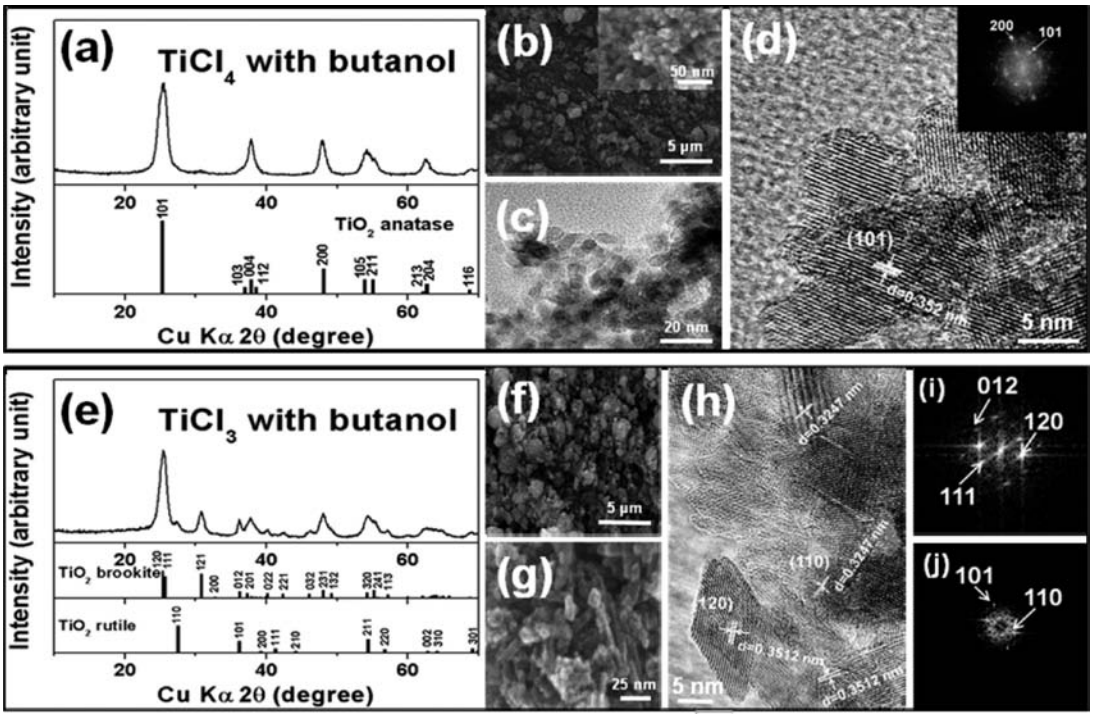

Figure 3. (a) XRD pattern, (b) SEM image, and (c and d) TEM and FFT images of the TiO_2 nanoparticles synthesized with $TiCl_4$ and butanol, and (e) XRD pattern, (f and g) SEM images, (h) TEM images, and (I and j) FFT images of TiO_2 nanorods synthesized with $TiCl_3$ and butanol.

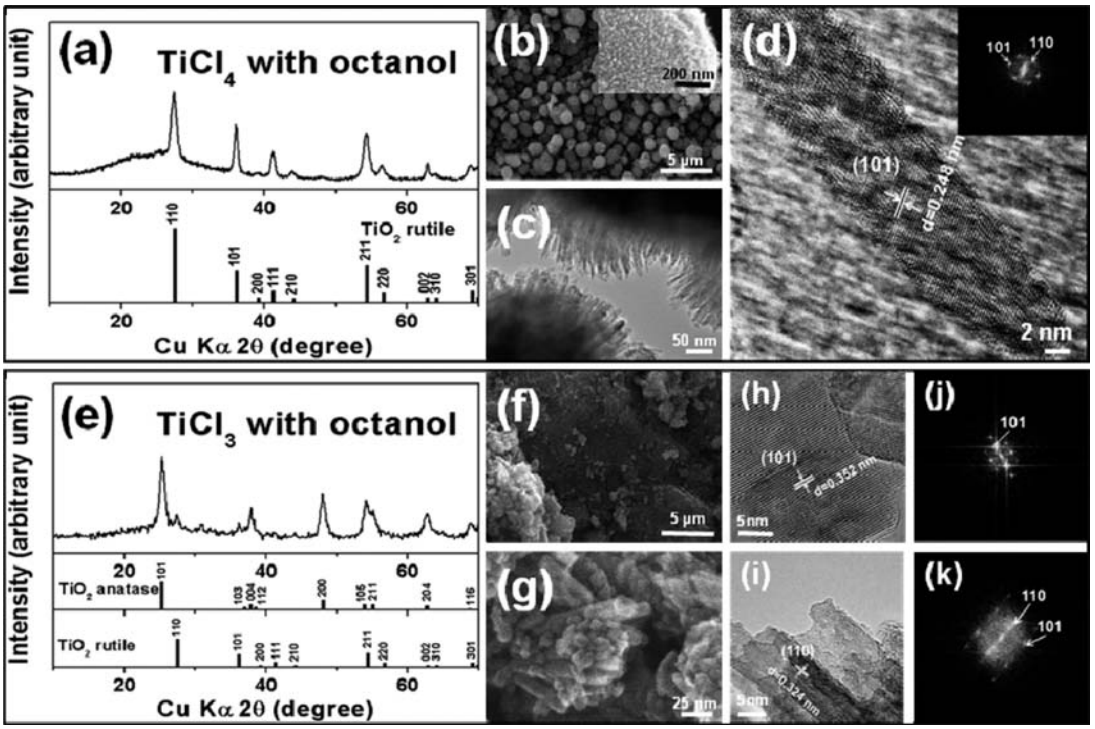

Figure 4. (a) XRD pattern, (b) SEM image, and (c and d) TEM and FFT images of the TiO_2 spheres synthesized with $TiCl_4$ and octanol, and (e) XRD pattern, (f and g) SEM images, (h and i) TEM images, and (j and k) FFT images of the TiO_2 nanoparticle and nanorods synthesized with $TiCl_3$ and octanol.

to its larger size. Figure 3a shows the XRD pattern of the as-synthesized sample obtained with $TiCl_4$. All reflections could be assigned to the tetragonal anatase TiO_2 ($I4_1/amd$, JCPD 21-1272). The mean crystallite size D_{101} is ~6.3 nm. The SEM and TEM images shown in Figure 3b and 3c reveal nanoparticles with an average size of ~8 nm. The HRTEM image in Figure 3d reveals an average domain size of ~10 nm, and the lattice fringe with the *d*-spacing value of 0.352 nm corresponds to the (101) plane of anatase TiO_2. The inset in Figure 3d shows the FFT image of the anatase TiO_2 nanoparticles and a set of sharp spots related to the (101), (004), and (200) planes of the anatase phase.

dx.doi.org/10.1021/ic202239n | *Inorg. Chem.* 2012, 51, 3505–3512

On the other hand, the XRD pattern of the as-synthesized sample prepared with $TiCl_3$ in Figure 3e shows orthorhombic brookite TiO_2 (*Pcab*, JCPD 29-1360) and a small amount of tetragonal rutile TiO_2 ($P4_2/mnm$, JCPD 84-1284). The SEM images in Figure 3f and 3g indicate brookite TiO_2 nanorods with a thickness and length of, respectively, ~ 10 and ~40 nm and rutile TiO_2 nanoparticles with a particle size of 10−25 nm. The TEM image in Figure 3h shows agglomerated brookite TiO_2 nanorods and rutile TiO_2 nanoparticles with good crystallinity. The lattice fringe with a *d* spacing of 0.3512 nm corresponds to the (120) plane of brookite TiO_2 and with a *d* spacing of 0.3247 nm corresponds to the (110) plane of rutile TiO_2. The FFT images in Figure 3i and 3j give a set of sharp spots corresponding to, respectively, the (120), (111), and (012) planes of the brookite phase and the (110) and (101) planes of the rutile phase. As mentioned before, it is known that the residual alkoxy groups determine the crystallization behavior of TiO_2 precursors,[27,29] and the crystallization behavior is probably most influenced by the initial ultrastructure of the amorphous precursor.[30] Crystallization of brookite might be related to unique formation of hydroxyl groups in the reaction of butanol with $TiCl_3$. This formation may be due to the increased cationic character on the tertiary carbon atom of butanol that favors the nucleophilic attack of chloride ions as

$$\equiv TiCl + BuOH \rightarrow \equiv TiOH + BuCl$$

The last set of experiments was carried out with octanol. Octanol also does not mix homogeneously with $TiCl_4$ or $TiCl_3$ under mild stirring due to its much larger size. Figure 4a shows the XRD pattern of the as-synthesized sample obtained with $TiCl_4$, and all reflections could be assigned based on the tetragonal rutile TiO_2 ($P4_2/mnm$, JCPD 84-1284). The mean crystallite size D_{110} is ~8.5 nm. The SEM image in Figure 4b reveals spherical morphology with an average size of ~1 μm. Figure 4c presents the TEM image of rutile TiO_2 spheres built with nanorods on the surface with a thickness and length of, respectively, ~10 and ~100 nm. Interestingly, the large surface area of the nanorod building spheres may be beneficial to reduce the diffusion pathways for ionic and electronic transport and increase the power density. The HRTEM image in Figure 4d shows a single nanorod, and the lattice fringe with a *d*-spacing value of 0.248 nm corresponds to the (101) plane of rutile. The FFT image in Figure 4d presents a set of sharp spots corresponding to the (110) and (101) planes of the rutile phase.

The XRD patterns of the as-synthesized sample prepared with $TiCl_3$ shows tetragonal anatase TiO_2 ($I4_1/amd$, JCPD 21-1272) and a small amount of tetragonal rutile TiO_2 ($P4_2/mnm$, JCPD 84-1284). The SEM images in Figure 4f and4g reveal a mixture of TiO_2 nanoparticles and nanorods with a particle size of 20−50 nm. The TEM images in Figure 3h and 3i reveal well-crystallized anatase TiO_2 nanoparticles and rutile TiO_2 nanorods with the lattice fringe *d* spacing of 0.352 nm corresponding to the (101) plane of anatase TiO_2 and 0.324 nm corresponding to the (110) plane of rutile TiO_2. The FFT image in Figure 3j and 3k shows a set of sharp spots corresponding, respectively, to the (101) planes of the anatase phase and (110) and (101) planes of the rutile phase.

As seen above, our MW-ST synthesis process with the various alcohol media and $TiCl_4$ vs $TiCl_3$ precursors gives various polymorphs and morphologies of TiO_2: spheres with $TiCl_4$ and ethanol, nanoparticles with $TiCl_4$ and propanol, mixture of nanorods and nanoparticles with $TiCl_3$ and butanol, and nanorod building spheres with $TiCl_4$ and octanol. To have a better characterization of the surface area and porous nature of the various TiO_2 polymorphs and morphologies, N_2 adsorption−desorption isotherms were collected as shown in Figure 5. The BET method was used to calculate the specific

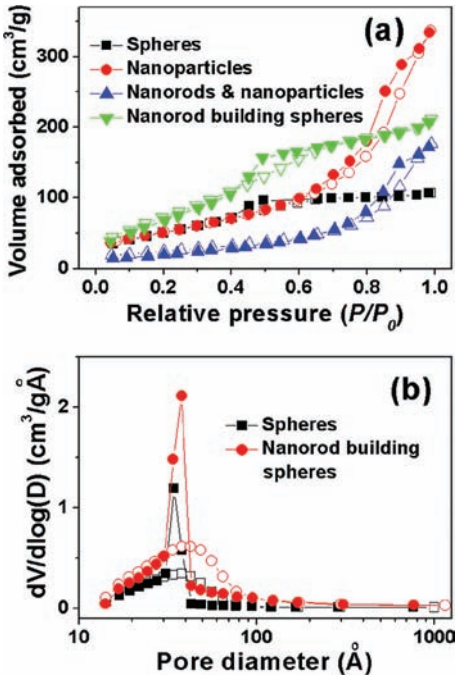

Figure 5. (a) Nitrogen adsorption−desorption isotherms and (b) BJH pore size distribution plots of the TiO_2 samples.

area and pore size distribution from the adsorption−desorption isotherms based on the Barrett−Joyner−Halenda (BJH) method. The nitrogen adsorption−desorption isotherms show similar type IV curves, and the hysteresis loop is between the H1 and H2 types.[31] The BET surface areas of the spheres, nanoparticles, mixture of nanorods and nanoparticles, and nanorod building spheres are, respectively, 222, 215, 94, and 404 m^2/g. Large hysteresis loops with shapes that are intermediate between the typical H1- and H2-type isotherms are observed for these mesoporous TiO_2 samples. Such strong hysteresis is believed to be related to the capillary condensation associated with the large pore channels but may also be due to the modulation of the channel structure.[32] The BJH pore size distributions for the sphere and the nanorod building sphere samples demonstrate the presence of well-developed mesoporosity with very narrow pore size distributions, with an average pore diameter ranging from 4 to 8 nm. The high BET surface area and large porosity also illustrate the nanostructured morphology of the samples. These nanostructured morphologies may allow rapid filling by the electrolyte within the TiO_2 particles during the electrochemical charge/discharge reaction, enhancing the rate capability of the samples.

Theses results demonstrate that the crystalline form and morphology of the TiO_2 nanomaterials are strongly dependent on the titanium precursor and solvent properties.[13,27−29,33] In our MW-ST process, there is a lot of dissolved HCl in the alcohols by forming oxonium salts. The dissolved HCl may act as a catalyst for etherification of the alcohols. Water is produced as a byproduct during the etherification reaction, and it can act

dx.doi.org/10.1021/ic202239n | *Inorg. Chem.* 2012, 51, 3505−3512

as an oxygen donor during synthesis of TiO_2, covering the hydroxyl groups on the TiO_2 surface. The dissolved HCl as a byproduct during hydrolysis of $TiCl_4$ (or $TiCl_3$) in the hydrolytic process controls the crystal structure and crystallite size. It acts not only as a catalyst during the hydrolysis reaction but also as a constituent in preventing particle growth or agglomeration by electrostatic repulsion and delaying the gelation process. The reaction between $TiCl_4$ (or $TiCl_3$) and the alcohol becomes less vigorous with the increase in the number of carbon atoms in the alcohol, so does the evolution of HCl. The steric hindrance of the alcohols increases with increasing number of carbon atoms in the alcohols, causing replacement of chloride ions in $TiCl_4$ (or $TiCl_3$) by the alkoxy group more difficult. Consequently, the reaction system involves etherification of alcohols and production of water as a byproduct.[27,33] Accordingly, the crystal structure of the as-prepared nanocrystalline TiO_2 changes from anatase to rutile or brookite with increasing number of carbon atoms.

3.2. Electrochemical Properties. Figure 6 compares the first charge−discharge profiles of the TiO_2 samples prepared with $TiCl_4$ and various alcohols. The samples prepared with ethanol, propanol, and butanol exhibit first discharge and charge capacities of, respectively, ∼300 and 210 mAh/g, implying an initial Coulombic efficiency of 70%. The large irreversible capacity is caused by the −OH or ═C═O groups from the residual solvent present in the particles. Although the Coulombic efficiency could be increased by heating the samples at higher temperatures, it led to degradation of the other electrochemical performance parameters. The voltage profile exhibits a monotonic decrease from 2.5 to 1.75 V corresponding to storage of 0.1 lithium ion during the first discharge, which is close to the value expected for a monolayer of lithium on the surface of the TiO_2 particles. It is a common phenomenon related to the small crystallite size of nanosized materials. On the other hand, the sample prepared with $TiCl_4$ and octanol, which is rutile phase, shows first discharge and charge capacities of, respectively, 372 and 238 mAh/g, implying an initial Coulombic efficiency of 64%. As mentioned in the Introduction, only a small amount of lithium could generally be inserted into the bulk rutile TiO_2 in a galvanostatic mode. However, as the particle size decreases, more and more lithium could be electrochemically reacted with rutile.[4,5,12] The initial discharge capacity of 372 mAh/g observed with our sample corresponds to insertion of 1.1 lithium, but part of this capacity is due to reaction of the residual −OH or ═C═O groups and electrolyte decomposition on the surface of the electrode.

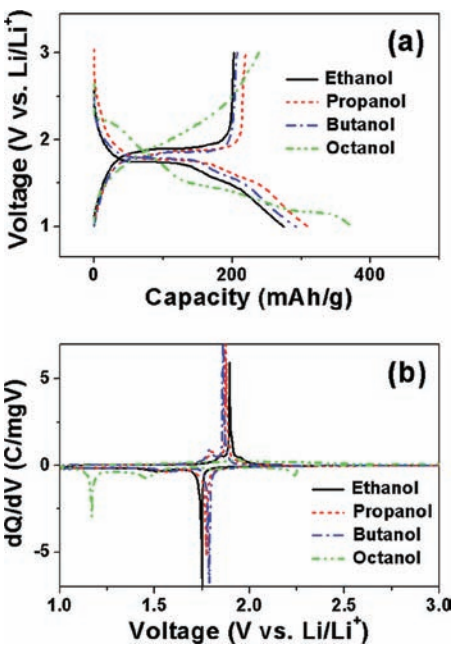

Figure 6. Comparison of the (a) discharge−charge profiles and (b) differential capacity plots (DCPs) of the TiO_2 samples synthesized with $TiCl_4$ in various alcohol (ethanol, propanol, butanol, and octanol) media.

The differential capacity plots (DCP) in Figure 6b display features characteristic of the voltage plateaus during discharge and charge, respectively, at around 1.75 and 1.9 V, which correspond to the known biphasic process (Li-poor phase and Li-rich phase) of the lithium insertion/extraction into/from anatase TiO_2 (samples obtained with $TiCl_4$ and ethanol, propanol, or butanol). Anatase has a tetragonal structure (space group $I4_1/amd$) with the Ti^{4+} ions at the 4a octahedral sites and the O^{2-} ions at the 8e sites. The lithium ions are inserted into the empty 4b octahedral sites during discharge.[34] While anatase is known to insert generally only about 0.5 lithium, the nanostructured TiO_2 obtained by the microwave-solvothermal process described here inserts ∼0.9 lithium, increasing the specific capacity significantly. On the other hand, DCP for the rutile TiO_2 (sample obtained with $TiCl_4$ and ocatnol) exhibits three anodic peaks at 2.23, 1.46, and 1.17 V vs Li/Li^+ during discharge, corresponding to solid−solution-type transitions and biphasic processes.[5,12] Koudrichova et al.[35,36] calculated the preferential insertion of lithium into the octahedral sites to be by 0.7 eV/Li. Although Li insertion into rutile TiO_2 is thermodynamically favorable, bulk TiO_2 under ordinary electrochemical conditions shows low reactivity with lithium due to the dense close packing of the structure and consequent kinetic restrictions. Interestingly, the Li^+-ion diffusion could be enhanced significantly with decreasing crystallite size, resulting in insertion of ∼1.1 lithium into the TiO_2 particles.

Figure 7 shows the first discharge−charge profiles and DCPs of the TiO_2 samples synthesized with $TiCl_3$ and various alcohols. Although the samples synthesized in the propanol and octanol media with $TiCl_3$ have a small amount of brookite and rutile TiO_2 phases as indicated by the XRD data, the voltage profiles of the samples synthesized in the ethanol, propanol, and ocatanol media with $TiCl_3$ exhibit voltage profiles similar to those prepared with $TiCl_4$. However, the sample synthesized with butanol has slightly lower first discharge and charge capacities of, respectively, 252 and 153 mAh/g due to the presence of the brookite TiO_2 phase. The discharge capacity of brookite TiO_2 is lower than that of rutile and anatase and matches with the previously reported results.[13,32] The DCPs of brookite and ananatse TiO_2 show a major pair of the anodic peak (during discharge) and cathodic peak (during charge) at, respectively, around 1.75 and 1.9 V. The capacities of the brookite and anatase TiO_2 phases are related to insertion of lithium into the channels caused by the TiO_6 octahedral arrangement along [001] and [010] directions, respectively, in the brookite and anatase phases.[37] It has been reported that the lithium insertion properties of the anatase phase are generally much better than those of the brookite phase, although the size and morphology of the TiO_2 polymorphs are also important controlling factors.

Figure 8a and 8b compare the cyclability at 1−3 V at a constant current (30 mA/g) (C/10 rate) of the as-synthesized

dx.doi.org/10.1021/ic202239n | Inorg. Chem. 2012, 51, 3505−3512

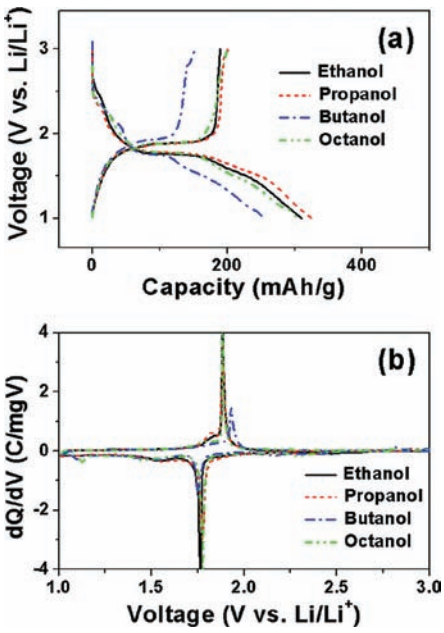

Figure 7. Comparison of the (a) discharge−charge profiles and (b) DCPs of the TiO_2 samples synthesized with $TiCl_3$ in various alcohol (ethanol, propanol, butanol, and octanol) media.

samples prepared with the $TiCl_4$ and $TiCl_3$ precursors in various alcohol media. While the as-synthesized samples prepared with $TiCl_4$ in propanol and butanol media and with $TiCl_3$ in ethanol, propanol, and octanol media exhibit a slowly capacity fade, the TiO_2 samples prepared with $TiCl_4$ in ethanol and octanol media and with $TiCl_3$ in butanol medium show good cyclability. Particularly, the sample synthesized with $TiCl_4$ in octanol exhibits excellent cyclability, retaining 91% of the capacity after 100 cycles. Clearly, the particle morphology influences the electrochemical performance. For example, the nanorod-building spherical-type particles could make a better dispersion during the electrode casting process, and its mesoporosity provides a higher surface contact between the active material and the electrolyte, resulting in improved electroactivity. Also, a smooth accommodation of the strain occurring during the lithium insertion process by the mesoporosity and nanostructural morphology leads to much better cyclability.

Figure 8c and 8d compares the rate capabilities of the as-synthesized samples prepared with $TiCl_4$ and $TiCl_3$ in various alcohols at various C rates from 0.1C to 5C rates. The TiO_2 sample prepared with $TiCl_4$ in octanol shows excellent rate capability. In particular, it retains a high capacity of ∼165 and 142 mAh/g, respectively, at 3C and 5C rates with stable cycling.

4. CONCLUSION

Three different polymorphs of TiO_2 (anatase, rutile, and brookite) have been obtained by a novel microwave-assisted solvothermal process with the $TiCl_4$ or $TiCl_3$ precursors in various alcohol (ethanol, propanol, butanol, and octanol) media. Ti/Cl ion concentration, reaction pH, and size of the alcohol molecule are found to influence the morphology, crystal structure, and crystallite size of the TiO_2 particles formed. Particularly, the rutile TiO_2 spheres built up of nanorods that were obtained with $TiCl_4$ in octanol medium exhibit a high capacity of >200 mAh/g with excellent cycle life and rate capability. The nanorod-building morphology with a small crystallite size and large surface area provides good electrical contact and accommodate the strain occurring during the charge−discharge process smoothly, resulting in facile lithium-ion diffusion and superior electrochemical performance. The study demonstrates that control of the reaction medium and precursors play a critical role on the nanomorphology and lithium storage properties of TiO_2.

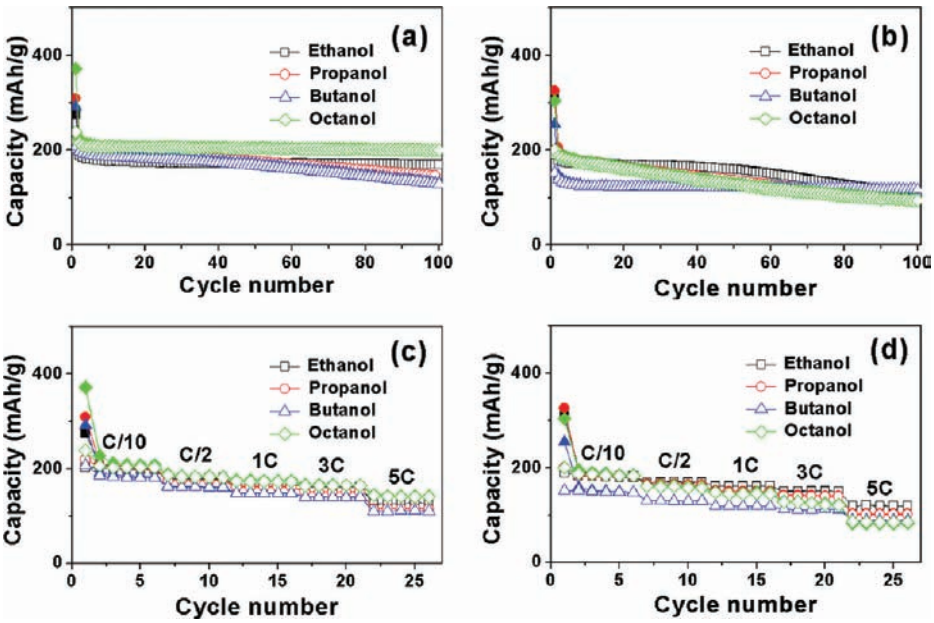

Figure 8. Comparison of the (a) cyclability of the TiO_2 samples synthesized with $TiCl_4$ in various alcohol media, (b) cyclability of the TiO_2 samples synthesized with $TiCl_3$ in various alcohol media, (c) capacity retention at various C rates, illustrating the rate capability of the TiO_2 samples synthesized with $TiCl_4$ in various alcohol media, and (d) capacity retention at various C rates, illustrating the rate capability of the TiO_2 samples synthesized with $TiCl_3$ in various alcohol media.

dx.doi.org/10.1021/ic202239n | *Inorg. Chem.* 2012, 51, 3505−3512

AUTHOR INFORMATION

Corresponding Author

*Phone: (512) 471-1791. Fax: (512) 471-7681. E-mail: rmanth@mail.utexas.edu.

ACKNOWLEDGMENTS

This work was supported by the Department of Energy Office of Basic Energy Science grant number DE-SC0005397 and the Welch Foundation grant F-1254. The authors thank Mr. Ki-Youl Yoon for his help with the BET measurements.

REFERENCES

(1) Huggins, R. A. *Solid State Ionics* **1998**, *113*, 57.
(2) Pacholski, C.; Kornowski, A.; Weller, H. *Angew. Chem., Int. Ed.* **2002**, *41*, 1188.
(3) Kuhn, A.; Amandi, R.; García-Alvarado, F. *J. Power Sources* **2001**, *92*, 221.
(4) Sudant, G.; Baudrin, E.; Larcher, D.; Tarascon, J.-M. *J. Mater. Chem.* **2005**, *15*, 1263.
(5) Reddy, M. A.; Kishore, M. S.; Pralong, V.; Caignaert, V.; Varadaraju, U. V.; Raveau, B. *Electrochem. Commun.* **2006**, *8*, 1299.
(6) Lakshmi, B. B.; Patrissi, C. J.; Martin, C. R. *Chem. Mater.* **1997**, *9*, 2544.
(7) Wang, C. C.; Ying, J. Y. *Chem. Mater.* **1999**, *11*, 3113.
(8) Cozzoli, P. D.; Korrowski, A.; Weller, H. *J. Am. Chem. Soc.* **2003**, *125*, 14539.
(9) Wagemaker, M.; Kearley, G. J.; Well, A. A. van; Mutka, H.; Mulder, F. M. *J. Am. Chem. Soc.* **2003**, *125*, 840.
(10) Zukalová, M.; Kalbá, M.; Kavan, L.; Exnar, I.; Graetzel, M. *Chem. Mater.* **2005**, *17*, 1248.
(11) Guo, Y.-G.; Hu, Y.-S.; Maier, J. *Chem. Commun.* **2006**, 2783.
(12) Baudrin, E.; Cassaignon, S.; Koelsch, M.; Jolivet, J.-P.; Dupont, L.; Tarascon, J.-M. *Electrochem. Commun.* **2007**, *9*, 337.
(13) Dambournet, D.; Belharouak, I.; Amine, K. *Chem. Mater.* **2010**, *22*, 1173.
(14) Sushko, M. L.; Rosso, K. M.; Liu, J. *J. Phys. Chem. Lett.* **2010**, *1*, 1967.
(15) Beuvier, T; Richard-Plouet, M.; Granvalet, M. M.-L.; Brousse, T.; Crosnier, O.; Brohan, L. *Inorg. Chem.* **2010**, *49*, 8457.
(16) Okumura, T.; Fukutsuka, T.; Yanagihara, A.; Orikasa, Y.; Arai, H.; Ogumi, Z.; Uchimoto, Y. *Chem. Mater.* **2011**, *23*, 3636.
(17) Yildirim, H.; Greeley, J.; Sankaranarayanan, S. K. R. S. *J. Phys. Chem. C* **2011**, *115*, 15661.
(18) Buonsanti, R.; Carlino, E.; Giannini, C.; Altamura, D.; Marco, L. D.; Giannuzzi, R.; Manca, M.; Gigli, G.; Cozzoli, P. D. *J. Am. Chem. Soc.* **2011**, *133*, 19216.
(19) Davis, M. E. *Nature* **2002**, *417*, 813.
(20) Maier, J. *Nat. Mater.* **2005**, *5*, 805.
(21) Bruce, P. G.; Scrosati, B.; Tarascon, J.-M. *Angew. Chem., Int. Ed.* **2008**, *47*, 2930.
(22) Kim, S.-W; Han, H. T.; Kim, J; Gwon, H.; Moon, H.-S.; Kang, S.-W.; Kim, S. O.; Kang, K. *ACS Nano* **2009**, *3*, 1085.
(23) Gerbec, J. A.; Magana, D.; Washington, A.; Strouse, G. F. *J. Am. Chem. Soc.* **2005**, *127*, 15791.
(24) Li, G. H.; Zheng, Y. F.; Ma, C. A. *Chinese J. Inorg. Chem.* **2005**, *21*, 1231.
(25) Cheng, H.; Ma, J.; Zhao, Z. G.; Qi, L. M. *Chem. Mater.* **1995**, *7*, 663.
(26) Yin, H.; Wada, Y.; Kitamura, T.; Sumida, T.; Hasegawa, Y.; Yanagida, S. *J. Mater. Chem.* **2002**, *12*, 378.
(27) Arnal, P.; Corriu, R. J. P.; Leclercq, D.; Mutin, P. H.; Vioux, A. *J. Mater. Chem.* **1996**, *6*, 1925.
(28) Kominami, H.; Kohno, M.; Kera, Y. *J. Mater. Chem.* **2000**, *10*, 1151.
(29) Jolivet, J.-P.; Cassaignon, S.; Chanéac, C.; Chiche, D.; Tronc, E. *J. Sol-Gel Sci. Technol.* **2008**, *46*, 299.
(30) In *Ultrastructure Processing of Advanced Ceramics*; Mackenzie, J. D., Ulrich, D. R., Eds.; Wiley: New York, 1988.
(31) Kruk, M.; Jaroniec, M. *Chem. Mater.* **2001**, *13*, 3169.
(32) Yang, P.; Zhao, D.; Margolese, D. I.; Chmelka, B. F.; Stucky, G. D. *Nature* **1998**, *396*, 152.
(33) Wang, C.; Deng, Z.-X.; Zhang, G.; Fan, S.; Li, Y. *Powder Technol.* **2002**, *125*, 39.
(34) Ohzuku, T.; Kodama, T.; Hirai, T. *J. Power Sources* **1985**, *14*, 153.
(35) Koudriachova, M. V.; Harrison, N. M.; Leeuw, S. W. *Phys. Rev. Lett.* **2001**, *86*, 1275.
(36) Koudriachova, M. V.; Harrison, N. M.; Leeuw, S. W. *Phys. Rev. B* **2002**, *65*, 235423.
(37) Jin, Y.-H.; Lee, S.-H.; Shim, H.-W.; Ko, K. H.; Kim, D.-W. *Electrochim. Acta* **2010**, *55*, 7315.